Optimisation of the additive manufacturing parameters of polylactic acid (PLA) cellular structures for biomedical applications

Myers, David; Abdelwahab, Adel; Hafeez, Farrukh; Kovacev, Nikolina; Essa, Khamis

DOI:
10.1016/j.jmbbm.2022.105447

Document Version
Publisher's PDF, also known as Version of record

Citation for published version (Harvard):
Myers, D, Abdelwahab, A, Hafeez, F, Kovacev, N & Essa, K 2022, 'Optimisation of the additive manufacturing parameters of polylactic acid (PLA) cellular structures for biomedical applications', *Journal of the Mechanical Behavior of Biomedical Materials*, vol. 136, 105447. https://doi.org/10.1016/j.jmbbm.2022.105447

journal of the mechanical behavior of biomedical materials 136 (2022) 105447

Contents lists available at ScienceDirect

Journal of the Mechanical Behavior of Biomedical Materials

journal homepage: www.elsevier.com/locate/jmbbm

Optimisation of the additive manufacturing parameters of polylactic acid (PLA) cellular structures for biomedical applications

David Myers, Adel Abdel-Wahab *, Farrukh Hafeez, Nikolina Kovacev, Khamis Essa

Department of Mechanical Engineering, School of Engineering, University of Birmingham, Edgbaston, Birmingham, B15 2TT, UK

ARTICLE INFO

Keywords:
Additive manufacturing (AM)
Fused deposition modelling (FDM)
Cellular structures
Biodegradable polylactic acid (PLA)
Orthopaedics scaffolds
Schoen gyroid
Schwarz primitive

ABSTRACT

Fused deposition modelling (FDM) is an additive manufacturing technology used to create functional and complex geometries directly from computer-generated models. This technique can be utilised to generate cellular structures with controllable pore size, pore shape, and porosity. Cellular structures are fundamental in orthopaedics scaffolds because of its low elastic modulus, high compressive strength, and adequate cell accommodation spaces. This paper aims at investigating and optimising the FDM additive manufacturing process parameters of polylactic Acid (PLA) for two lattice structures namely Schoen Gyroid and Schwarz Primitive. The effect of additive manufacturing critical process parameters including layer height, flow rate, and print speed on the geometrical accuracy and compressive strength of the specimens were analysed. In addition, other parameters that have minimal effect on the geometrical accuracy of the printed parts were discussed. A Full Factorial Analysis (FFA) using Minitab software was undertaken to identify the perfect combination of printing parameters to provide the most geometrically accurate structure. In this study, samples of the Schoen Gyroid and the Schwarz Primitive lattices and a solid control cylinder were 3D printed using the ideal printing combination to assess the manufacturability, the geometrical accuracy, and the mechanical behaviour of both designs. It was found that the optimised FDM process parameters for the studied cellular structures were a layer height of 0.16 mm, a printing speed of 50 mm/s and a flow rate of 90%. As a result of using these parameters, the solid, Schoen Gyroid and Schwarz Primitive specimens demonstrated elastic moduli values of 951 MPa, 264 MPa, and 221 MPa, respectively. In addition, the Schoen Gyroid and the Schwarz Primitive have reached their stress limits at around 8.68 MPa and 7.06 MPa, respectively. It was noticed that the Schoen Gyroid structure exhibited ~ 18% higher compressive strength and ~ 16% higher elastic modulus compared to the Schwarz Primitive structure for the same volume fraction of porosity, overall dimensions, and the manufacturing process parameters. Although both structures revealed mechanical properties that fall within the range of the human trabecular bone, but Schoen Gyroid exhibited improved structural integrity performance that is evident by its post-yield behaviour.

1. Introduction

Additive manufacturing (AM) is a revolutionary new technology allowing new shapes and structures to be manufactured that were previously impossible using traditional methods. The biomedical field has many applications that can benefit from these new manufacturing solutions (Brambilla et al., 2021; Hassanin et al., 2016; Langford et al., 2021). For instance, orthopaedics implants can be designed to imitate several aspects of bone tissues such as the structure, elastic modulus, mechanical strength, biocompatibility, and bone ingrowth (Aimar et al., 2019a; Gómez et al., 2016; Weiner et al., 1999). Nevertheless, the direct use of bulk materials is not recommended for bone implants since the difference in the stiffness between the host bone and the implant leads to bone resorption due to stress shielding and stress concentration (Poltue et al., 2021). Therefore, cellular structures have been integrated into the design of implants for orthopaedics. Nonetheless, the design of cellular-based orthopaedics scaffolds remains a challenge due to the complex interrelationship among their geometrical characteristics, mechanical performance, and biological behaviour (Jeon et al., 2014; Poltue et al., 2021).

There are various AM processes that have potential biomedical applications (Elsayed et al., 2019; Read et al., 2015; Tan et al., 2019). In

* Corresponding author.
E-mail addresses: dxm689@alumni.bham.ac.uk (D. Myers), a.a.m.abdelwahab@bham.ac.uk (A. Abdel-Wahab), f.hafeez@bham.ac.uk (F. Hafeez), NXK889@student.bham.ac.uk (N. Kovacev), k.e.a.essa@bham.ac.uk (K. Essa).

https://doi.org/10.1016/j.jmbbm.2022.105447
Received 7 May 2022; Received in revised form 21 August 2022; Accepted 1 September 2022
Available online 9 September 2022

particular, FDM technology was introduced since the early 90s by Stratasys Inc., USA (Minetola et al., 2016), and is capable of creating highly innovative and complex parts with suitable mechanical properties. FDM can make complex parts directly from computer-generated CAD files, and it can be used for commercially available materials such as acrylonitrile butadiene styrene (ABS), polycarbonate (PC), and polylactic acid (PLA) (Aimar et al., 2019b; Elsayed et al., 2019; El-Sayed et al., 2020). PLA is a biodegradable, rigid, and non-toxic polymer that can be manufactured without harmful solvents (Fatyeyeva et al., 2017). FDM is the main AM process to print parts with PLA. In FDM technology, a thermoplastic filament is heated to a semi-liquid state (170 °C–240 °C) and extruded from a nozzle onto a heated bed, layer by layer along a controlled path (Gebhardt et al., 2019). The use of PLA with its biocompatible properties manufactured by FDM could prove to be an ideal solution for interaction surfaces and would expand the research currently carried out around utilising lattice structures in orthopaedics.

The wide range of applications for AM in the biomedical field has been expanded by the biocompatibility of lactic acid-based polymers such as (PLA) (Calignano et al., 2019). A biocompatible material can be defined as a material that is compatible with living tissue or living system by not being toxic or injurious to the living tissue and not causing an adverse immune response. In addition, it requires the compound to support interaction between the living cells and the material (Ramot et al., 2016). The biocompatibility and safety of PLA has been investigated by Ramot et al. (2016) and Middleton and Tipton (2000), concluding PLA is safe to use in implants. This is further verified in a study by Singh et al. (2019) showing apatite (the mineral component that makes up human bones (Vallet-Regí and Arcos Navarrete, 2016)) forming on the surface of PLA test subjects with basic lattice structures (Singh et al., 2019).

By utilising lattice structures created by AM from biocompatible materials, orthopaedics scaffolds that mimic the structure of bone tissues can be realised. As a result, the printed scaffolds can imitate various aspects of the structure of bone including elastic modulus, mechanical strength, biocompatibility, and bone ingrowth (Gómez et al., 2016; Weiner et al., 1999). In particular, mechanical strength and bone ingrowth are the essential in orthopaedics (K. C. K. C. Nune et al., 2017; K C K C Nune et al., 2017; Ran et al., 2018). Effective bone ingrowth has significant effect on the rate of revisions, and the main factors affecting the bone ingrowth are porosity, pore size, pore shape, and the random distribution of the pores (Warnke et al., 2009). When the porous structure has suitable porosity and pore size, it offers enough space for cell proliferation (Kuboki et al., 2001; Zadpoor, 2015). These factors are directly linked to the geometrical accuracy of the AM technology and the optimisation of the manufacturing process parameters. With the development of AM, these factors can be controlled by computer-aided designs in advance. As a result, the stress shielding effect can be effectively reduced when the elastic modulus of the scaffolds is similar to that of the bone (Chen et al., 2020).

Triply Periodic Minimal Surface (TPMS) scaffolds have recently been the focus on many researchers because of their potential to be used as orthopaedics implants (Poltue et al., 2021). For instance, healing of large-scale bone defects due to diseases, accidents, and surgeries is not possible without effective and safe implants that can facilitate bone growth and be compatible with the surrounding bone tissues. The implicit nature of TPMS-based scaffolds allows for precise control of important physical characteristics such as pore size, elastic properties, surface-to-volume ratio, and fluid flow behaviour (Poltue et al., 2021). As a result, TPMS porous structures offer the opportunity to optimise both the mechanical and biological properties of bone implants. Researchers have promising results for TPMS-based as opposed to strut-based scaffolds (Chen et al., 2020; Hsieh et al., 2021). A recent study investigated the interconnection among structures, mechanical properties, biological performance, and manufacturing limitations for a number of TPMS-based structures including Primitive, Gyroid, Diamond, Neovius, FRD and IWP (Poltue et al., 2021). It was concluded that the choice of the TPMS model affects significantly important features such as pore size, elastic properties, and flow behaviour. In addition, they found that some TPMS-based structures such as the Primitive structure exhibited lower modulus at low relative density while FRD exhibited lower modulus at high density. The remaining structures including Gyroid, Diamond, Neovius, and IWP exhibited comparable mechanical properties for both low and high relative densities. In an *in-vitro* study, TPMS-based structure, Gyroid, was compared with scaffolds with random pore architectures. It was found that Gyroid showed superior performance in terms of permeability and seedability (Melchels et al., 2010). In addition, Ma et al. (2020) carried out an experimental study on additively manufactured Gyroid scaffolds and considered different aspects including manufacturability, permeability, mechanical behaviours, and biocompatibility. They found that a Gyroid scaffolds that matches human trabecular bone can be obtained by altering their design parameters. Besides, they noticed a significant effect of permeability on initial cell growth.

The use of the biocompatible PLA polymer coupled with a lattice structure could improve the interaction between the implant and the surrounding bone structure, thus reducing stress shielding. Improving the manufacturing quality of this is very important to get the desired interaction between bone tissue and implant.

Various FDM additive manufacturing parameters affect the quality of the printed parts, but the technology has high potential and viability when these parameters are optimised and successfully controlled. Hence, it is crucial to control and optimise these parameters during manufacturing (Ahn et al., 2002; Casavola et al., 2016).

Based on the above literature review, various attempts have been made to study cellular structures such as Schoen Gyroid and Schwarz Primitive; however, based on the author's knowledge there are no evidence in the literature of analysing the effect of FDM additive manufacturing critical process parameters including layer height, flow rate, and print speed on the geometrical accuracy and compressive strength of these structures. A Full Factorial Analysis (FFA) using Minitab software was undertaken to identify the optimised combination of printing parameters to provide the most geometrically accurate structure.

In order to achieve the main aim of this research, the following objectives have been identified: choosing the most suitable material and additive manufacturing process for the requirements of the prototype; designing unit cell versions of the Schoen Gyroid, Schwarz Primitive, and control solid body to initially validate the proposal; selecting the slicing software and the key printing variables that affect geometrical accuracy; conducting a FFA using Minitab software to find the optimum printing parameters that can accurately produce a repeatable 3D model of the cellular structure (Minitab, 2021a); manufacturing the cellular structures and the control solid body and analysing the quality of the prints; and finally testing the optimised cellular structures and comparing their compression behaviours with the control solid body.

2. Materials and methods

2.1. Unit cell proof of concept

Based on literature it was decided the Schoen Gyroid and the Schwarz Primitive structures are among the most promising candidates for orthopaedics scaffolds. Therefore, these structures will be compared with a solid body to analyse the volume fractions, weights, manufacturing costs, and elastic-plastic behaviours when loaded in compression to identify the most mechanically-sound structure for a prototype orthopaedics implant. The following method shows how this will be carried out.

Proof of concept study for the Schoen Gyroid unit cell structure has been designed using SolidWorks (see Fig. 1a). The design was duplicated using the linear pattern tool, to create a (2 × 2 x 2 assembly) version of the unit cell. This was saved as an industry standard (.stl file) and sliced

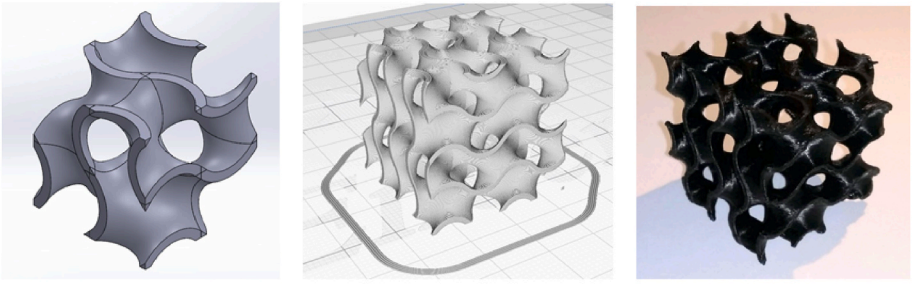

Fig. 1. a) SolidWorks model of Schoen Gyroid unit cell, b) sliced model of Schoen Gyroid unit cell using Ultimaker Cura software, and c) validation print of the design.

using the Ultimaker Cura software (see Fig. 1b) to create a G-code file (Ultimaker, 2010). The G-code file contains all the parameters required to print a part. These include nozzle temperature, layer height, and the path the printer will follow. A verification print of the Schoen Gyroid design (see Fig. 1c) was printed from PLA on a Creality Ender 3 Pro FDM printer (see Fig. 2) (Creality, 2014). Similarly, unit cells were designed and printed for the Schwarz Primitive and a solid body control unit cell, see Fig. 3. These initial prints proved the concept that each design was printable without failure.

2.2. Optimising process parameters

In the Ultimaker Cura software (Ultimaker, 2010), the printing parameters can be tuned to optimise prints for a specific printer, filament, and application. It is critical that the geometrical accuracy of the prints is maximised as this would affect the accuracy of the prototype's porosity, pore size and pore shape. Besides, it is also important to consider both the printing time and the cost of the print.

After running several preliminary FFA tests using Minitab software, it was identified that there are three critical printing parameters that influence the geometrical accuracy of a given print: layer height (mm), flow rate (%) and print speed (mm/s). With four further parameters having a minor effect on the geometrical accuracy: nozzle temperature (°C), build plate temperature (°C), travel speed (mm/s) and retraction distance (mm). A FFA Test using Minitab software was conducted to optimise the critical parameters, where each parameter had three levels (low, medium, and high), see Table 1 (Minitab, 2021a). The other parameters were set to Cura's Creality Ender 3 Pro profile and kept constant (Ultimaker, 2010); see Table 1 for a breakdown of these parameters.

The first critical parameter, layer height, changes the thickness of each layer that is printed and impacts the resolution of the specimen. While a lower layer height increases the resolution, it also increases the time to print, cost and potentially the mechanical performance of the part (Garzon-Hernandez et al., 2020; Mwema and Akinlabi, 2020). The minimum layer height for the Ender 3 Pro is 0.12 mm increasing in steps equal to the size of the extruder nozzle of 0.04 mm. The second critical parameter, flow rate, changes the rate at which the filament is extruded.

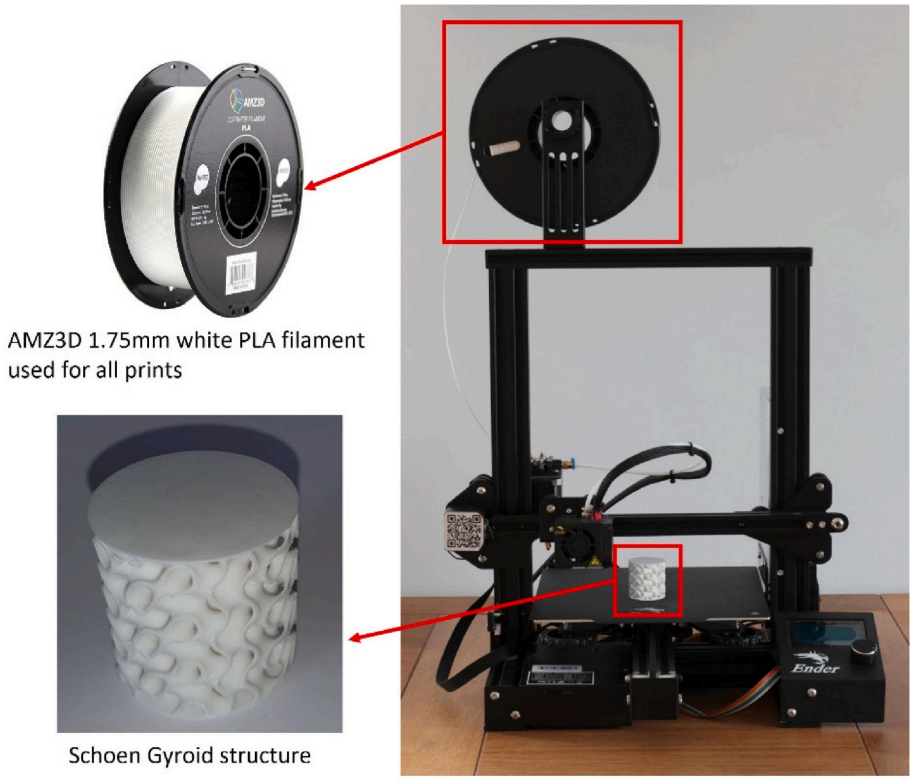

Fig. 2. Creality Ender 3 Pro FDM used for all prints and AMZ3D 1.75 mm white PLA filament used for all prints.

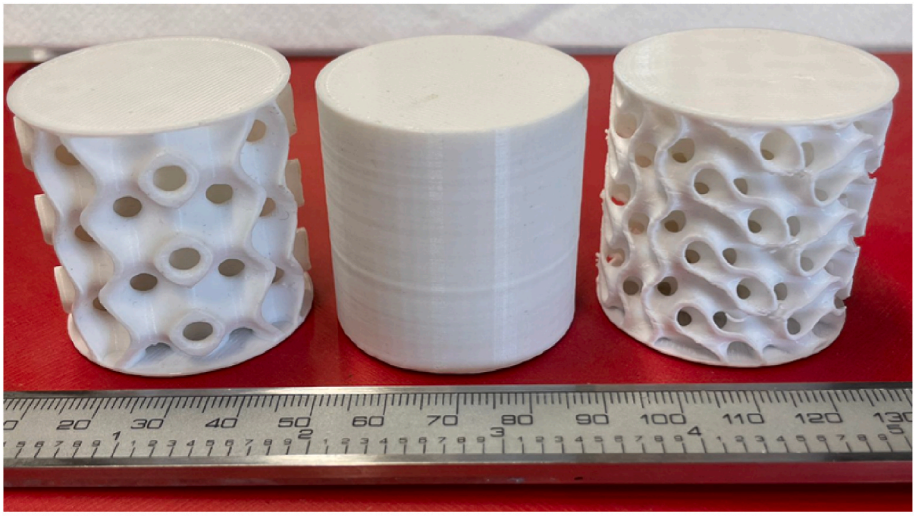

Fig. 3. 3D printed specimens of a) Schwarz Primitive structure, b) solid control cylinder, and c) Schoen Gyroid structure.

Table 1
Printing parameters used in the full factorial analysis.

Critical Parameters	Level 1	Level 2	Level 3
Layer height (mm)	0.12	0.16	0.2
Flow rate (%)	90	100	110
Print speed (mm/s)	40	50	60
Other Parameters	Fixed Level		
Nozzle temperature (°C)	197		
Build plate temperature (°C)	55		
Retraction distance (mm)	6		
Travel speed (mm/s)	150		

With an infill of 100%, the printer often extrudes too much molten filament; this causes each layer to bulge with geometrical inaccuracies (Mwema and Akinlabi, 2020). Therefore, optimising the flow rate will improve the accuracy of the geometrical dimensions. However, if the flow rate is insufficient, spaces within the layers could form. This causes layer adhesion problems and impacts on the mechanical integrity of the print (Mwema and Akinlabi, 2020). The third critical parameter, print speed, affects the velocity at which the nozzle moves while extruding. Increasing this velocity would reduce printing times; however, this may also affect layer adhesion with a chance of introducing imperfections and printing failures. The print speed for the Ender 3 Pro ranges from 1 mm/s to 200 mm/s; however, speeds greater than 70 mm/s often cause the prints to fail (Creality, 2014).

The four further parameters that also have a minor effect on accuracy of the print are discussed in the following paragraph.

The first parameter, nozzle temperature, defines the temperature the filament is heated to when extruded from the nozzle. A sufficient temperature is required to melt the filament to ensure that the nozzle does not get blocked (Mwema and Akinlabi, 2020). An optimum nozzle temperature improves the bonds between the layers, thus reducing failures occurring especially at overhangs. The PLA filament used for testing has a specified nozzle temperature range (180 °C–210 °C). The optimum value of the second parameter, build plate temperature, improves the adhesion between the build plate and the model, reducing printing failures and warping (Mwema and Akinlabi, 2020).

With FDM printers, melted filament is not drawn back from the nozzle when traveling between printing locations. Therefore, an unwanted thin line of filament can often join these locations, this is known as stringing. The third parameter, retraction distance, has the main impact on the stringing of the filament. Retraction reduces the pressure in the nozzle melting zone; therefore, reducing the amount of filament extruded when traveling. The fourth parameter, travel speed, changes the velocity of the extruder when the printer is not extruding; therefore, optimising this will reduce stringing and could marginally improve printing times.

Considering both the critical and further parameters, the FFA using Minitab Software (Minitab, 2021a) produced twenty-seven tests for various printing input parameters, see Table 2. For each of the twenty-seven runs described by the Full Factorial Test, a single unit cell of the Schwarz Primitive was printed, see Fig. 4. The outputs from this test were the average outer dimensions of the test specimen and its strut diameter. These outputs were measured and averaged, and as a result, the geometrical accuracy was determined for each test specimen. The

Table 2
Full factorial test of various printing input parameters.

Run	Layer Height (mm)	Flow Rate (%)	Print Speed (mm/s)	Mean Outer Dimensions (mm)			Mean Strut Dimensions (mm)
				X	Y	Z	
1	0.12	90	40	15.01	15.04	16.24	3.01
2	0.12	90	50	15.02	15.03	16.23	3.01
3	0.12	90	60	15.03	15.09	16.24	3.01
4	0.12	100	40	15.17	15.17	16.27	3.04
5	0.12	100	50	15.19	15.22	16.28	3.02
6	0.12	100	60	15.23	15.27	16.29	3.03
7	0.12	110	40	15.46	15.54	16.31	3.18
8	0.12	110	50	15.45	15.46	16.31	3.14
9	0.12	110	60	–	–	–	–
10	0.16	90	40	15.00	15.06	16.23	3.02
11	0.16	90	50	15.03	15.05	16.23	3.02
12	0.16	90	60	15.05	15.07	16.22	3.03
13	0.16	100	40	15.22	15.27	16.26	3.11
14	0.16	100	50	15.21	15.26	16.24	3.05
15	0.16	100	60	15.22	15.25	16.25	3.08
16	0.16	110	40	15.47	15.47	16.33	3.23
17	0.16	110	50	15.40	15.45	16.32	3.24
18	0.16	110	60	–	–	–	–
19	0.2	90	40	15.00	15.05	16.26	3.03
20	0.2	90	50	15.04	15.07	16.27	3.01
21	0.2	90	60	15.08	15.14	16.27	3.04
22	0.2	100	40	15.19	15.26	16.29	3.12
23	0.2	100	50	15.26	15.24	16.32	3.13
24	0.2	100	60	15.28	15.29	16.31	3.18
25	0.2	110	40	15.42	15.47	16.37	3.20
26	0.2	110	50	15.53	15.55	16.37	3.37
27	0.2	110	60	15.49	15.52	16.41	3.35

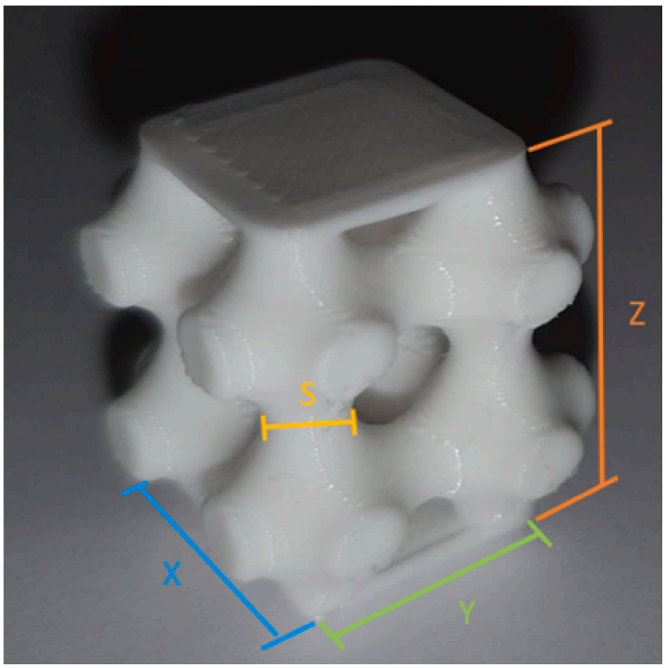

Fig. 4. Example Schwarz Primitive test run with measured output dimensions: X is the depth; Y is the width; and Z is the height of the test specimen; S is the strut diameter.

Schwarz Primitive design was chosen for these tests as the design contains several features that can be easily defined and measured, with the measurements taken using a digital vernier calliper with an accuracy of ±0.02 mm.

The statistical analysis software Minitab was used to analyse the output results from the Full Factorial Test (Minitab, 2021a). The analysis comprises of an analysis of variance, a mean effects plot and an optimise parameters run. The analysis of variance describes the relationship between the individual input printing parameters and the various dependent output parameters to categorise the importance of each input. The mean effects plot visualises these relationships. Optimise parameters finds the best combination of each input parameter, to provide the best overall geometrical accuracy. Each combination is given a composite desirability, which rates the combination against its output geometrical accuracy. More details can be found in the results section. Printing times and total cost were then compared against the composite desirability to specify the perfect combination between layer height, flow rate, and print speed.

2.3. Manufacturing of unit cell prototypes

MATLAB software ("MathWorks," n.d.) was used to generate the cellular structures using the equations below for the lattice surfaces; Eq. (1) generates the Schoen Gyroid structure (Al-Ketan et al., 2020) with Eq. (2) generating the Schwarz Primitive structure (Jia et al., 2020). With the surface generated by v and a controllable offset generating the solid volume.

$$v = \sin x \cdot \cos y + \sin y \cdot \cos z + \sin z \cdot \cos x \quad \text{(Eq.1)}$$

$$v = \cos x + \cos y + \cos z \quad \text{(Eq.2)}$$

The MATLAB function "stlwrite" was used to generate.stl files, which could then be manipulated in SolidWorks software ("SolidWorks Software," 1995). Flat plates were added to the top and bottom to evenly distribute the load, see Fig. 3. These sample unit cells along with a solid control cylinder were then printed using run 11's optimum printing parameters (see Fig. 3 and Table 2). More details can be found in both the results and discussion sections.

2.4. Mechanical testing of unit cell prototypes

Compression tests of the Schoen Gyroid, Schwarz Primitive, and solid control cylinder specimens were carried out using a universal testing machine (Instron 4467, Instron, Norwood, MA, USA). The specimens and experimental setup are shown in Fig. 5a and b, respectively. The compression deformation rate was set to 1 mm/min for all the samples. The compression load was applied along the build direction for all the specimens with the compressive stress and strain obtained using the standard formulae.

3. Results

3.1. Minitab analysis of test prints

The geometrical accuracy of the twenty-seven test prints of the Schwarz Primitive lattice unit cell were measured. Table 2 provides a breakdown of the input parameters for each test and the measured geometrical outputs. As shown in Table 2, test runs 9 & 18 failed to print after multiple attempts, therefore the geometrical dimensions were impossible to measure. This data was entered into a FFA in Minitab (2021a). The test created an analysis of variance, which shows the interaction between the various input parameters, see Table 3.

The Total Degrees of Freedom (DF) are used to estimate the variability of the different parameters. The Adjusted Sums of Squares (Adj SS) are the measurements of the variation of each parameter. Adjusted Mean Squares (Adj MS) are the Adj SS measurements when considering the degrees of freedom of each parameter. The f-value is the test used to understand if a parameter is associated with the output response (Minitab, 2021a). These four outputs are used by Minitab to calculate the p-value of each input parameter. The lower the p-value the greater the effect the input parameter has on the output response. It is suggested that if the p-value is lower than 0.05 confidence threshold, then the input has a significant effect on the output response (Minitab, 2021a).

As can be seen from Table 3, flow rate has the most impact of the three input parameters with a p-value of 0.000, followed by the layer height with a p-value of 0.012. Print speed with a p-value of 0.617 can be regarded as having little impact on the geometrical accuracy of the test prints. Factorial Plots can then be plotted on the data, these are split into two graphs for each measured output. The Main Effects Plots (see Fig. 6) show if altering one input parameter has an impact on the measured output. If the line is horizontal, then changes in the input have no impact on the measured output. When the line is not horizonal there is an effect between altering the input and the measured output, this effect is known as the main effect. The steeper the gradient, the greater this main effect (Minitab, 2021a).

As shown in Fig. 6, the gradient of the flow rate lines is the steepest and very consistent. This shows that the flow rate has the greatest impact on each of the measured outputs, and thus the overall geometrical accuracy. This finding correlates with the p-value of the flow rate of 0.000. The fact that the lines are always relatively linear show the flow rate has a continuous relationship with each of the measured outputs (Minitab, 2021a).

The gradients of the layer height for outer X and Y are relatively flat, which shows that layer height does not have a significant effect on the X and Y dimensions of the test prints. However, the layer height has a large non-continuous effect on the outer Z dimensions of the print. The layer height also has a continuous relationship with the strut diameter, but the gradient of this line and therefore its effect on this output is lower compared to outer Z dimensions.

The gradient of the print speed lines for all measured outputs shown are all slightly horizontal, which shows that print speed has an overall limited impact on the geometrical accuracy of the test prints.

The Interaction Plots, see Fig. 7, show the relationship between two

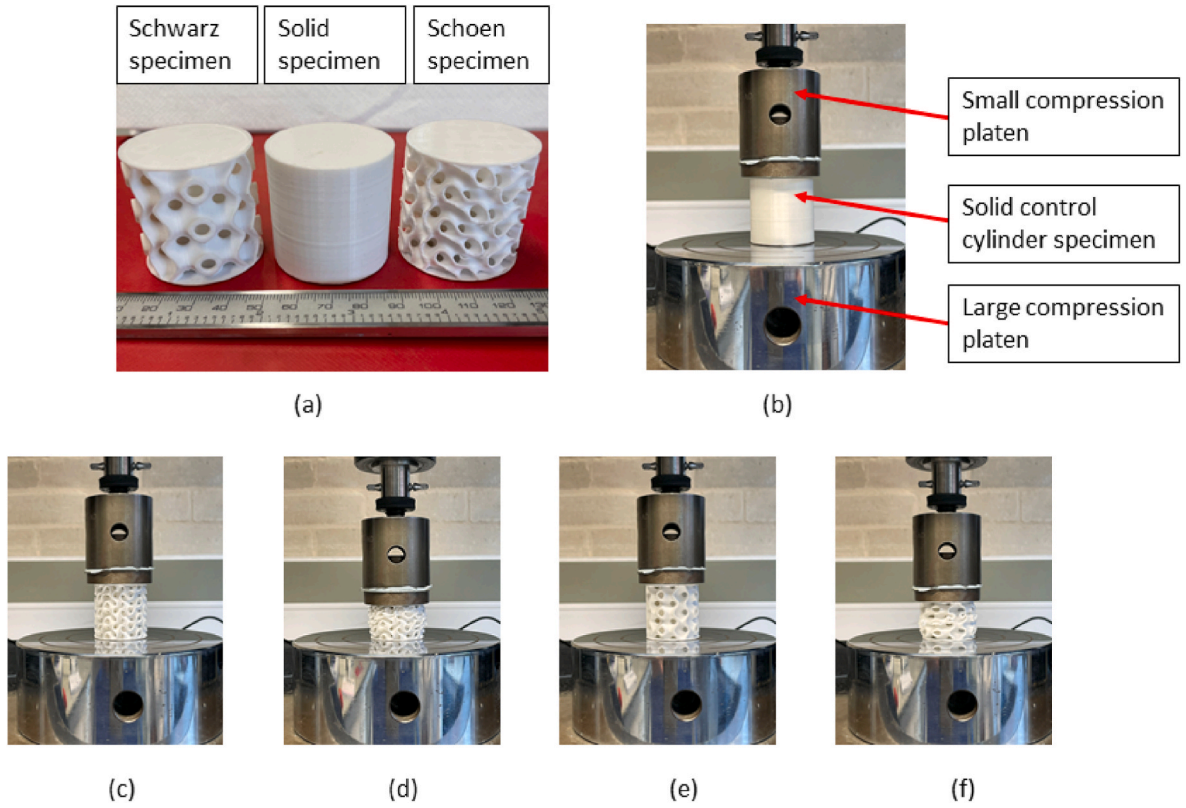

Fig. 5. a) Schwarz Primitive, solid control cylinder, and Schoen Gyroid compression test specimens, b) experimental setup of the compression test of the cellular specimens, c) Schoen Gyroid specimen before compression test, d) Schoen Gyroid specimen after compression test, e) Schwarz Primitive specimen before compression test, f) Schwarz Primitive specimen after compression test.

Table 3
Analysis of variance conducted on the full factorial test.

Source	DF	Adj SS	Adj MS	f-value	p-value
Model	18	0.2631	0.0146	10.67	0.004
Linear	6	0.2112	0.0352	25.70	0.000
Layer Height (mm)	2	0.0282	0.0141	10.29	0.012
Flow Rate (%)	2	0.1258	0.0629	45.92	0.000
Print Speed (mm/s)	2	0.0014	0.0007	0.52	0.617
2-Way Interactions	12	0.0223	0.0019	1.35	0.371
Layer Height (mm)* Flow Rate (%)	4	0.0101	0.0025	1.85	0.239
Layer Height (mm)*Print Speed (mm/s)	4	0.0055	0.0014	1.01	0.471
Flow Rate (%)*Print Speed (mm/s)	4	0.0045	0.0011	0.83	0.554
Error	**6**	**0.0082**	**0.0014**		
Total	**24**	**0.2713**			

input parameters with regards to a specific output parameter. If the lines are not parallel in the interaction plot, it shows there is some interaction between the two parameters. This means changing one parameter has an impact on the main effects of the other parameter. Therefore, if strong interaction occurs, analysis of the main effects must consider this interaction (Minitab, 2021a).

The lines in the interaction plots shown in Fig. 7 are all relatively parallel for each input. This means there is little interaction between the different input parameters for each measured output and the main effects plots can be analysed directly. The only interaction (slightly non-parallel lines) occurs between the layer height and print speeds mainly for the 40 mm/s line diverging slightly from both the 50 and 60 mm/s lines.

As seen in Table 4, a response optimiser was also executed on the data in Table 2 using Minitab Software (Minitab, 2021b). Target values of 16.2 mm × 15 mm x 15 mm for the outer X-, Y-, and Z-dimensions, respectively, and 3 mm for the strut were the inputs.

The composite desirability specifies how well the combination of all the input parameters satisfies the goals set. This value ranges from 0 to 1, where 1 represents the ideal case and 0 indicates at least one response from the input parameters is outside acceptable limits (Minitab, 2021a). The composite desirability measures the overall output response to a given combination. This is calculated using Eq. (3) (Minitab, 2021a) which takes an average of the desirability's of each of the individual measured outputs known as *individual desirability*.

$$D = (d_1 \times d_2 \times \cdots \times d_n)^{\frac{1}{n}} \quad \text{(Eq.3)}$$

Where:

- D = the composite desirability
- d_i = the individual desirability for the ith output measurement
- n = the number of output measurements

The individual desirability of each response to a given input combination is calculated using Eq. (4) if $L_i \leq \hat{y}_i \leq T_i$ or Eq. (5) if $T_i \leq \hat{y}_i \leq U_i$ (Minitab, 2021a).

$$d_i = \frac{\hat{y}_i - L_i}{T_i - L_i} \quad \text{(Eq.4)}$$

$$d_i = \frac{U_i - \hat{y}_i}{U_i - T_i} \quad \text{(Eq.5)}$$

Where:

- d_i = the individual desirability for the ith output measurement

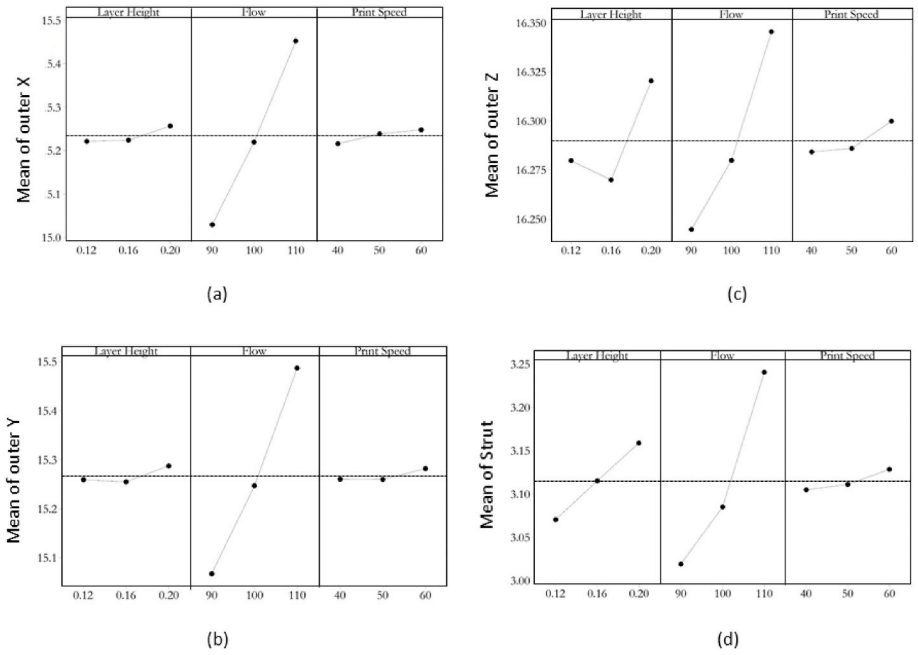

Fig. 6. Main Effects plots for a) the measured outer X-dimension, b) the measured outer Y-dimension, c) the measured outer Z-dimension, and d) the measured strut diameter.

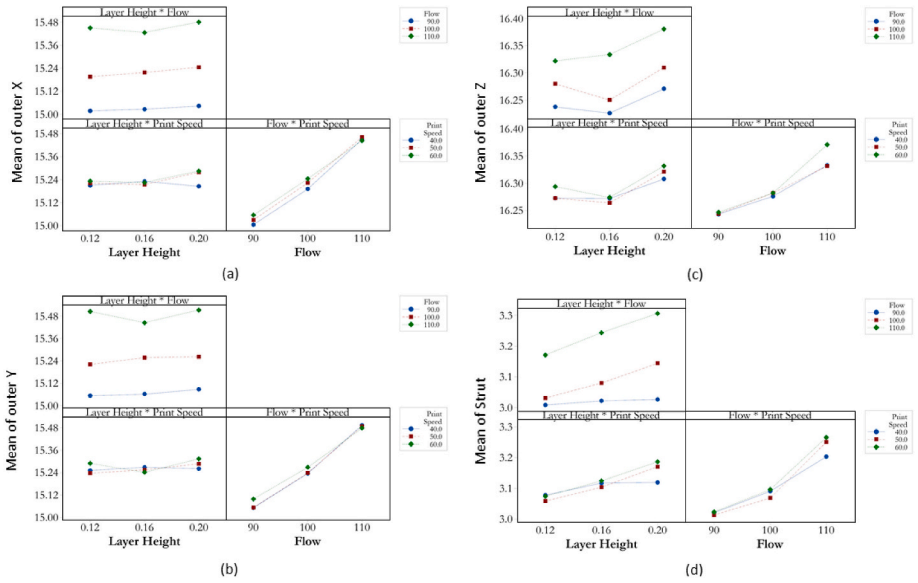

Fig. 7. Interaction plot for the measured a) Outer X-dimension, b) Outer Y-dimension, c) Outer Z-dimension, d) and the Strut diameter.

- $\widehat{y}_i$ = the predicted value of the ith output response
- T_i = the target value of the ith output response
- L_i = the lowest acceptable value of the ith output response
- U_i = the highest acceptable value of the ith output response

The individual desirability is a simple ratio of the difference between the predicted response and the lowest acceptable boundary, over the difference between the target response and the highest acceptable boundary. The composite desirability is then a combination of these ratios.

As shown in Table 4, there are seven different runs with a composite desirability of over 0.85, with run 2 being ideal in terms of the desirability of its geometrical accuracy. This solution has a layer height of 0.12 mm, a flow rate of 90% and a print speed of 50 mm/s.

3.2. Printing times and cost analysis

The energy used was monitored during one of the early test prints. It was found the Ender 3 Pro printer heated up for 5 min at 280 W upon the start of a print and repeated this for each hour of printing time. During the rest of the time, the printer ran at 60 W. As the individual prints take several hours, it can be assumed these reheats equalise over time. From this it was calculated the printer ran at an average power of 70 W (Creality, 2014).

The Cura slicer outputs the run time and the quantity of the filament used for each test print. This was used to calculate the energy consumption, filament cost and therefore total cost for each test run (Ultimaker, 2010).

Fig. 8 highlights the runs of a composite desirability of over 0.85,

Table 4
Response optimiser for full factorial test using minitab (Minitab, 2021a).

Solution	Run	Layer Height (mm)	Flow Rate (%)	Print Speed (mm/s)	Composite Desirability
1	2	0.12	90	50	0.936
2	11	0.16	90	50	0.934
3	1	0.12	90	40	0.921
4	12	0.16	90	60	0.911
5	10	0.16	90	40	0.893
6	19	0.20	90	40	0.889
7	3	0.12	90	60	0.878
8	20	0.20	90	50	0.813
9	21	0.20	90	60	0.777
10	5	0.12	100	50	0.707
11	4	0.12	100	40	0.692
12	14	0.16	100	50	0.678
13	15	0.16	100	60	0.656
14	6	0.12	100	60	0.641
15	13	0.16	100	40	0.641
16	22	0.20	100	40	0.606
17	23	0.20	100	50	0.516
18	24	0.20	100	60	0.481
19	17	0.16	110	50	0.271
20	18	0.16	110	60	0.262
21	8	0.12	110	50	0.257
22	16	0.16	110	40	0.244
23	7	0.12	110	40	0.238
24	9	0.12	110	60	0.205
25	25	0.20	110	40	0.187
26	26	0.20	110	50	0.083
27	27	0.20	110	60	0.000

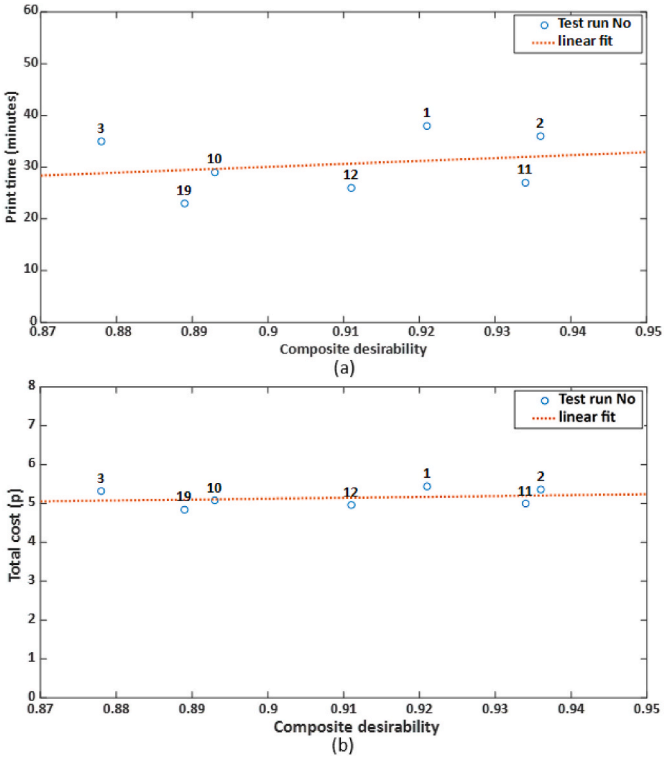

Fig. 8. a) Time to print against composite desirability for the runs with a composite desirability of over 0.85, and b) Total cost against composite desirability for the runs with a composite desirability of over 0.85.

showing a comparison between the printing time and total cost of the runs and their respective composite desirability.

There is a slight positive correlation between an increase in composite desirability with an increase in time to print and total cost. The percentage changes from maximum (run 1) to minimum (run 19) is 65.2% for the time taken to print and 10.5% for the total cost.

The percentage difference in composite desirability between runs 2 and 11 is only a 0.2% decrease (from 0.936 for run 2 to 0.934 for run 11); however, the savings in printing time from run 2 to run 11 is 25% and total cost savings are 7.3%. As a result, run 11 conditions were selected as ideal and used to print the lattice prototypes. These conditions are a layer height of 0.16 mm, a flow rate of 90% and a print speed of 50 mm/s.

3.3. Optimal manufacturing of unit cell prototypes

Specimens of the Schoen Gyroid structure, Schwarz Primitive structure, and solid control cylinder were 3D printed using the obtained optimal process parameters. Table 5 shows the volume fractions, weights and costs of the Schoen Gyroid structure, Schwarz Primitive structure, and solid control cylinder. The Density of PLA is 1.24 g/cm^3. Volume fraction of porosity (φ) is a ratio of the volume of the pores over the apparent total bulk volume that would be taken up (V_T = 64000 mm^3), see Eq. (6) (Espinal, 2012). The volume of the pores is calculated using the difference between the apparent total bulk volume (V_T) and the volume of the structure (V_S).

$$\varphi = \frac{V_T - V_S}{V_T} \tag{6}$$

The overall volume fraction of porosity describes the structure as a whole. A hollow structure would have a value close to 1 and a solid structure would give a value close to 0.

3.4. Mechanical testing of unit cell prototypes

Fig. 9 shows the stress-strain curves of the solid control cylinder, Schoen Gyroid, and Schwarz Primitive. Both the Schoen and Schwarz cellular structures demonstrated elastic-plastic behaviour when loaded in compression. However, the solid control cylinder demonstrated an elastic behaviour, and a higher loading was required to reach its plastic behaviour (outside the limits of the available load cell). Nevertheless, the solid control cylinder was still showing elastic behaviour even after the compression load was almost twice the load at which both the Schoen and Schwarz structures started to demonstrate plastic behaviour, see Fig. 9. The solid, Schoen Gyroid and Schwarz Primitive specimens demonstrated elastic moduli values of 951 MPa, 264 MPa, and 221 MPa, respectively. In addition, the Schoen Gyroid and the Schwarz Primitive have reached their stress limits at around 8.68 MPa and 7.06 MPa, respectively. It was noticed that the Schoen Gyroid structure exhibited ~ 18% higher compressive strength and ~ 16% higher elastic modulus compared to the Schwarz Primitive structure for the same volume fraction of porosity, overall dimensions, and the manufacturing process parameters.

4. Discussion

4.1. Minitab analysis of test prints

The two prints that failed during the tests were runs 9 and 18. These both had the same error, where one of the layers failed to adhere to the previous one. This failure can be seen in Fig. 10 which shows that half of

Table 5
Breakdown of the unit cell prints for each lattice structure design.

Structure	Overall volume fraction of porosity	Weight (g)	Time to Print	Cost (p)
Schoen Gyroid	0.617	21.51	6h 13m	53.4
Schwarz Primitive	0.614	21.68	5h 10m	50.5
Control Cylinder	0.000	56.10	5h 57m	125.8

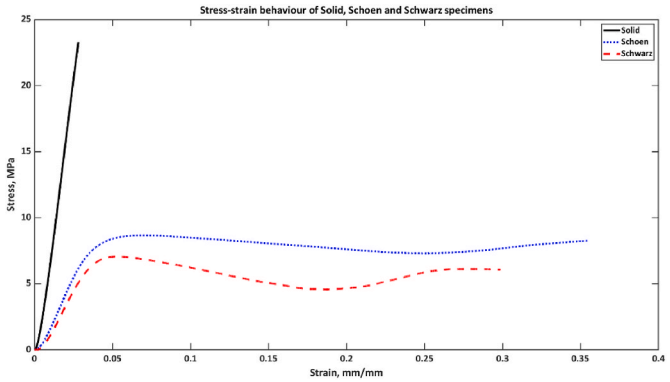

Fig. 9. Stress-strain behaviour of solid control cylinder, Schoen Gyroid, and Schwarz Primitive cellular structures.

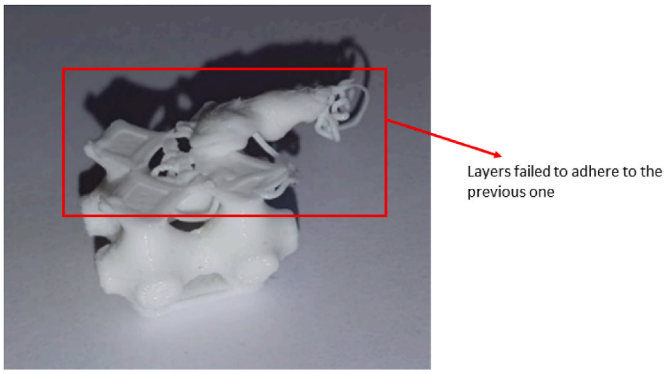

Fig. 10. Failed Test print for run 9.

the print is satisfactory up to the layer that failed.

These runs had both a flow rate of 110% and a print speed of 60 mm/s, suggesting these are factors that caused the prints to fail. A high flow rate such as 110% causes the filament to be over extruded. As seen in Table 4, the runs with 110% flow rate produced on average 5.9% over the target dimensions. This over extrusion often puts additional stress on the newly adhered layer. As was explained earlier, an increased print speed also causes adhesion problems between the layers. This combination of reduced layer adhesion and increased force on these layers may be the cause of the prints failing at a certain point of the print. Overall, it can be assumed that 60 mm/s exceeds the threshold to safely print the lattice structures consistently without failing.

In the analysis of variance, see Table 3, the p-value of a parameter is the probability that the parameter provides evidence against the null hypothesis (Minitab, 2021a). This is a hypothesis that suggests there is no statistical evidence between the relationship of the input parameter and the measured output (Haldar, 2018). Therefore, a lower p-value suggests there is stronger relationship between the variance of an input parameter and the output.

The flow rate is the most influential parameter that effects the geometrical accuracy of the test prints with a p-value of 0.000, see Table 3. This is backed up by the main effects plots with steep continuous lines for the flow rate graphs, see Fig. 6. This is a result of the flow rate directly changing the extrusion rate, with a lower flow rate causing under extrusion (geometrical dimensions are smaller) and higher flow rates causing over extrusion (geometrical dimensions are larger).

Layer height is the next most important parameter with a p-value of 0.012 (see Table 3), mainly affecting the accuracy of the Z-dimension and the strut diameter. The slicer works by dividing the required height by the specified layer height, and the resulting number of layers must be rounded to an integer. This means the height of the print in the G-code that the printer reads may not be the same as the original *.stl model entered into the Cura slicer (Ultimaker, 2010). This explains the non-continuous relationship between layer height and the outer Z-dimension shown in the main effects outer Z-dimension and strut plots, see Fig. 6c and d. The continuous relationship between layer height and strut diameter is a result of a smaller layer height creating a finer resolution on the prints curves. This means the minimum strut diameter can be closer to the target minimum diameter of 3 mm with lower layer heights. This trend is shown in Fig. 6d.

Print speed has the smallest effect and is outside the main effects p-value confidence threshold of 0.05 with a p-value of 0.617, see Table 3. This is because the print speed mainly changes printing times and layer adhesion rather than the geometrical accuracy.

With a 100% flow rate, prints are often over extruded due to the compression of layers. Therefore, to offset this and improve the geometrical accuracy a lower flow rate is required. It was found that 90% was ideal in this case. With the flow rate being the most influential parameter, the composite desirability of the runs was initially sorted in terms of their flow rate, with the top 9 runs having this ideal flow rate, see Table 4. The order is then ranked in terms of layer height with this being the second most important variable. On average for the prints with an ideal flow rate (90%) a layer height of 0.16 mm is the most accurate with an average composite desirability of 0.917. This is compared to a layer height of 0.12 mm with an average composite desirability of 0.912 and a layer height of 0.2 mm with an average composite desirability of 0.827, see Table 4. As the steepest main effects plots for the layer height is non-continuous (see Fig. 6), the closest to the target in this graph (0.16 mm) on average provides the most accurate layer height. With there being a slight interaction between layer height and print speed, the 0.16 mm layer height is not always the most accurate, requiring a combination of layer height and print speed.

4.2. Printing times and cost analysis

Fig. 8 shows runs with a composite desirability of over 0.85 where there are three key printing time levels. These can be categorised by runs with a time of between 20 and 25 min, 25–30 min, and 35–40 min, respectively. These correspond to the three levels of layer height, with the most time consuming being 0.12 mm requiring more layers to be printed. The variations in each layer are down to the variations in print speed with higher speeds reducing the time taken.

The current cost of a unit of domestic electricity in the UK (1 kWh) is nominally 20p. Combined with the average energy consumption for the test prints of 0.06 kWh means a very low energy cost of 1.2p. A larger contribution towards the cost of the print is the amount of filament material used. On average 0.62 m of filament was used for the test prints, at a cost of 6.3 p/m means the average material cost was 3.9p. The percentage of the overall cost due to the filament was 77.4% and energy consumed was 22.6%.

The only process parameter with an impact on the amount of filament material used is the flow rate. This factor directly changes the amount of filament being extruded at a given time, with higher flow rates using more filament. The top 9 most desirable combinations had the same flow rate; therefore, these all had the same filament cost, see Table 5.

The Energy consumed by the Ender 3 Pro printer is directly related to the printing time of each run. Therefore, any reductions in printing time because of increasing layer height or print speeds will directly reduce the energy consumed. However, as the energy consumed has a lower contribution to the cost, the improvement in terms of cost savings is much lower using the second most desirable run (run 11) over the first (run 2). This results in a cost saving of 7.3% compared to a printing time saving of 25%, see Fig. 8.

When the runs are scaled up to the typical size used in orthopaedics scaffolds, the printing run times go from on average 28 min to a few folds more. While keeping the same consumption trends the energy

consumed, and filament is dramatically increased. Run 11's combination of time savings and cost benefits even with a slight decrease in geometrical accuracy of 0.21% compared to run 2, show it is ideal combination of input parameters. Therefore, this combination consisting of a layer height of 0.16 mm, a flow rate of 90%, and a print speed of 50 mm/s, will be used for the full-scale test prints of the lattice structures.

4.3. Optimal manufacturing of unit cell prototypes

Both lattice structures demonstrated a significant reduction in both weight and cost compared to the solid control cylinder. The Schoen Gyroid structure had a 61.7% weight reduction and 57.6% cost reduction, whereas the Schwarz Primitive had a weight reduction of 61.3% and a 59.8% reduction in cost. Both these designs have a great potential for improving bone scaffolds. They reduce the cost of manufacture while saving weight to improve the patients' quality-of-life.

While there was a reduction in energy consumed for the Schwarz Primitive of 13.2% compared to the control, there was a minor increase for the Schoen Gyroid of 4.5%. This could be due to the Schoen Gyroid having a much more complicated structure and layer pattern, which takes more time to print each layer compared to both the control and the Schwarz Primitive structures.

A similar volume fraction of porosity, created by the 3D printing process, was used between the two designs to be able to accurately compare manufacturability with the variable porosity chosen. The ideal volume fraction would ensure the elastic modulus of the structure matches that of human bone. This should mean the implant avoids taking load from the surrounding bone. This is a common problem with current implants with under loading in human bones causing stress shielding problems.

4.4. Mechanical testing of unit cell prototypes

For both the Schoen Gyroid and Schwarz Primitive lattice structures, the stress-strain behaviours displayed overall gradual development of a plateau, which suggest a uniform load-carrying capacity of the unit cells, see Fig. 9. For the Schoen Gyroid structure, after reaching the compressive strength point, the stress-strain behaviour started to slightly concave down demonstrating a ductile failure without catastrophic failure of the unit cells. This indicates that the unit cells demonstrated a gradual load-carrying capacity or load distribution to different connecting struts of the connected unit cells, see Fig. 5 c and d. On the other hand, the Schwarz Primitive structure showed a steeper concave curve after reaching the maximum compressive strength point indicating a brittle failure where some unit cells collapsed or fractured suddenly and completely, see Fig. 5 e and f. As the compression test continues, other connecting cells started to carry the load, and as a result, they were subject to higher compressive stresses, this is evident by the increase in the stress level towards the end of the Schwarz Primitive stress-strain curve, see Fig. 9.

Trabecular bone demonstrates variation in their elastic properties as functions of apparent density and architecture; elastic modulus and strength values can vary by as much as 100-fold and 5-fold, respectively. Typically, the elastic modulus of human trabecular bone ranges between 10 and 3000 MPa and the strength ranges between 0.1 and 30 MPa (Morgan et al., 2018).

Although both structures revealed mechanical properties that fall within the range of the human trabecular bone, but Schoen Gyroid exhibited better structural integrity performance that is evident by its post-yield behaviour.

5. Conclusion

- The use of additive manufacturing has enabled the manufacture of both the Schoen Gyroid and Schwartz Primitive structures. There are further cost savings from utilising these lattice structures over the control cylinder. Additive manufacturing will also enable the implant to be specifically customised to each patient both in terms of size and its inbuilt mechanical properties.
- A critical factor for current additive manufacturing techniques especially the FDM process is the time required to print. Therefore, any reduction in the time taken to print implants will improve the viability of manufacturing prototype implants at full scale. The accuracy of the print will affect the porosity and therefore the effectiveness of the implant's ability to interact with surrounding bone structure. Run 11's printing time improvements along with a high geometrical accuracy shows it is ideally suited to meet these criteria.
- For both the Schoen Gyroid and Schwarz Primitive lattice structures, the stress-strain behaviours demonstrated overall gradual development of a plateau, which suggest a uniform load-carrying capacity of the unit cells. For the Schoen Gyroid structure, demonstrates a ductile failure without catastrophic failure of the unit cells. On the other hand, the Schwarz Primitive structure demonstrated a brittle failure where some unit cells collapsed or fractured suddenly and completely.

Funding

No funding has been received to carry out this work.

CRediT authorship contribution statement

David Myers: Writing – original draft, Visualization, Validation, Methodology, Investigation, Formal analysis, Data curation, Conceptualization. **Adel Abdel-Wahab:** Writing – review & editing, Validation, Supervision, Project administration, Methodology, Investigation, Formal analysis, Conceptualization. **Farrukh Hafeez:** Writing – review & editing, Supervision, Project administration, Methodology, Formal analysis, Conceptualization. **Nikolina Kovacev:** Visualization, Validation, Resources, Investigation, Data curation. **Khamis Essa:** Writing – review & editing, Validation, Supervision, Resources, Project administration, Methodology, Investigation, Formal analysis, Conceptualization.

Declaration of competing interest

The authors declare that they have no known competing financial interests or personal relationships that could have appeared to influence the work reported in this paper.

Data availability

Data will be made available on request.

Nomenclature

D	the composite desirability
d_i	the individual desirability for the ith output measurement
n	the number of output measurements
d_i	the individual desirability for the ith output measurement

$\widehat{y}_i$ the predicted value of the ith output response
T_i the target value of the ith output response
L_i the lowest acceptable value of the ith output response
U_i the highest acceptable value of the ith output response
φ Volume fraction of porosity
V_T total volume
V_S the volume of the structure

References

Ahn, S., Montero, M., Odell, D., Roundy, S., Wright, P.K., 2002. Anisotropic material properties of fused deposition modeling ABS. Rapid Prototyp. J. 8, 248–257. https://doi.org/10.1108/13552540210441166.

Aimar, A., Palermo, A., Innocenti, B., 2019a. The role of 3D printing in medical applications: a state of the art. vol. 2019, Article ID 5340616, 10 pages, 2019 J. Healthc Eng. 10, 2019.

Aimar, A., Palermo, A., Innocenti, B., 2019b. The role of 3D printing in medical applications: a state of the art. vol. 2019, Article ID 5340616, 10 pages, 2019 J. Healthc Eng. 10, 2019.

Al-Ketan, O., Lee, D.W., Rowshan, R., Abu Al-Rub, R.K., 2020. Functionally graded and multi-morphology sheet TPMS lattices: design, manufacturing, and mechanical properties. J. Mech. Behav. Biomed. Mater. 102, 103520 https://doi.org/10.1016/j.jmbbm.2019.103520.

Brambilla, C.R.M., Okafor-Muo, O.L., Hassanin, H., ElShaer, A., 2021. 3DP Printing of Oral Solid Formulations: A Systematic Review. Pharmaceutics. https://doi.org/10.3390/pharmaceutics13030358.

Calignano, F., Galati, M., Iuliano, L., Minetola, P., 2019. Design of additively manufactured structures for biomedical applications: a review of the additive manufacturing processes applied to the biomedical sector, 2019 J. Healthc Eng.. https://doi.org/10.1155/2019/9748212.

Casavola, C., Cazzato, A., Moramarco, V., Pappalettere, C., 2016. Orthotropic mechanical properties of fused deposition modelling parts described by classical laminate theory. Mater. Des. 90, 453–458. https://doi.org/10.1016/J.MATDES.2015.11.009.

Chen, H., Han, Q., Wang, C., Liu, Y., Chen, B., Wang, J., 2020. Porous scaffold design for additive manufacturing in orthopedics: a review. Front. Bioeng. Biotechnol. 8 https://doi.org/10.3389/fbioe.2020.00609.

Creality, 2014. Shenzhen creality 3D technology Co., ltd [WWW Document]. URL. https://www.creality.com/?spm=..product.header_1.1.

Elsayed, M., Ghazy, M., Youssef, Y., Essa, K., 2019. Optimization of SLM process parameters for Ti6Al4V medical implants. Rapid Prototyp. J. 25, 433–447. https://doi.org/10.1108/RPJ-05-2018-0112.

El-Sayed, M.A., Essa, K., Ghazy, M., Hassanin, H., 2020. Design optimization of additively manufactured titanium lattice structures for biomedical implants. Int. J. Adv. Manuf. Technol. 110, 2257–2268. https://doi.org/10.1007/s00170-020-05982-8.

Espinal, L., 2012. Porosity and its measurement. In: Characterization of Materials. American Cancer Society, pp. 1–10. https://doi.org/10.1002/0471266965.com129.

Fatyeyeva, K., Chappey, C., Marais, S., 2017. Biopolymer/clay nanocomposites as the high barrier packaging material: recent advances. Food Packaging 425–463. https://doi.org/10.1016/B978-0-12-804302-8.00013-3.

Garzon-Hernandez, S., Garcia-Gonzalez, D., Jérusalem, A., Arias, A., 2020. Design of FDM 3D printed polymers: an experimental-modelling methodology for the prediction of mechanical properties. Mater. Des. 188, 108414 https://doi.org/10.1016/J.MATDES.2019.108414.

Gebhardt, A., Kessler, J., Thurn, L., 2019. Additive manufacturing processes/3D printing. In: Gebhardt, A., Kessler, J., T.L (Eds.), 3D Printing. HANSER, pp. 33–70.

Gómez, S., Vlad, M.D., López, J., Fernández, E., 2016. Design and properties of 3D scaffolds for bone tissue engineering. Acta Biomater. 42, 341–350. https://doi.org/10.1016/J.ACTBIO.2016.06.032.

Haldar, S.K., 2018. No title. In: Haldar, S. (Ed.), Mineral Exploration. Elsevier, pp. 167–194.

Hassanin, H., Modica, F., El-Sayed, M.A., Liu, J., Essa, K., 2016. Manufacturing of Ti–6Al–4V micro-implantable parts using hybrid selective laser melting and micro-electrical discharge machining. Adv. Eng. Mater. 18, 1544–1549. https://doi.org/10.1002/adem.201600172.

Hsieh, M.T., Begley, M.R., Valdevit, L., 2021. Architected implant designs for long bones: advantages of minimal surface-based topologies. Mater. Des. 207, 109838 https://doi.org/10.1016/J.MATDES.2021.109838.

Jeon, H., Simon Jr., C.G., Kim, G., 2014. A mini-review: cell response to microscale, nanoscale, and hierarchical patterning of surface structure. J. Biomed. Mater. Res. B Appl. Biomater. 102, 1580–1594. https://doi.org/10.1002/jbm.b.33158.

Jia, H., Lei, H., Wang, P., Meng, J., Li, C., Zhou, H., Zhang, X., Fang, D., 2020. An experimental and numerical investigation of compressive response of designed Schwarz Primitive triply periodic minimal surface with non-uniform shell thickness. Extreme Mech Lett 37, 100671. https://doi.org/10.1016/j.eml.2020.100671.

Kuboki, Y., Jin, Q., Takita, H., 2001. Geometry of carriers controlling phenotypic expression in BMP-induced osteogenesis and chondrogenesis. J Bone Joint Surg Am 83-A Suppl, S105–S115.

Langford, T., Mohammed, A., Essa, K., Elshaer, A., Hassanin, H., 2021. 4D Printing of Origami Structures for Minimally Invasive Surgeries Using Functional Scaffold. Applied Sciences. https://doi.org/10.3390/app11010332.

Ma, S., Tang, Q., Han, X., Feng, Q., Song, J., Setchi, R., Liu, Ying, Liu, Yang, Goulas, A., Engstrøm, D.S., Tse, Y.Y., Zhen, N., 2020. Manufacturability, mechanical properties, mass-transport properties and biocompatibility of triply periodic minimal surface (TPMS) porous scaffolds fabricated by selective laser melting. Mater. Des. 195, 109034 https://doi.org/10.1016/J.MATDES.2020.109034.

MathWorks [WWW document], n.d. URL https://uk.mathworks.com/.

Melchels, F.P.W., Barradas, A.M.C., Van Blitterswijk, C.A., De Boer, J., Feijen, J., Grijpma, D.W., 2010. Effects of the architecture of tissue engineering scaffolds on cell seeding and culturing. Acta Biomater. 6, 4208–4217. https://doi.org/10.1016/J.ACTBIO.2010.06.012.

Middleton, J.C., Tipton, A.J., 2000. Synthetic biodegradable polymers as orthopedic devices. Biomaterials 21, 2335–2346. https://doi.org/10.1016/S0142-9612(00)00101-0.

Minetola, P., Iuliano, L., Marchiandi, G., 2016. Benchmarking of FDM machines through Part Quality using IT grades. Procedia CIRP 41, 1027–1032. https://doi.org/10.1016/J.PROCIR.2015.12.075.

Minitab, 2021a. Minitab 18 Statistical Software, vol. 18.

Minitab, 2021b. Minitab 18 Statistical Software, vol. 18.

Morgan, E.F., Unnikrisnan, G.U., Hussein, A.I., 2018. Annual review of biomedical engineering bone mechanical properties in healthy and diseased states. https://doi.org/10.1146/annurev-bioeng-062117.

Mwema, F., Akinlabi, E., 2020. Fused deposition modeling: strategies for quality enhancement. https://doi.org/10.1007/978-3-030-48259-6.

Nune, K.C., Kumar, A., Misra, R.D.K., Li, S.J., Hao, Y.L., Yang, R., 2017. Functional response of osteoblasts in functionally gradient titanium alloy mesh arrays processed by 3D additive manufacturing. Colloids Surf. B Biointerfaces 150, 78–88. https://doi.org/10.1016/J.COLSURFB.2016.09.050.

Nune, K.C., Misra, R.D.K., Li, S.J., Hao, Y.L., Yang, R., 2017. Cellular response of osteoblasts to low modulus Ti-24Nb-4Zr-8Sn alloy mesh structure. J. Biomed. Mater. Res. 105, 859–870. https://doi.org/10.1002/jbm.a.35963.

Poltue, T., Karuna, C., Khrueaduangkham, S., Seehanam, S., Promoppatum, P., 2021. Design exploration of 3D-printed triply periodic minimal surface scaffolds for bone implants. Int. J. Mech. Sci. 211, 106762 https://doi.org/10.1016/J.IJMECSCI.2021.106762.

Ramot, Y., Haim-Zada, M., Domb, A.J., Nyska, A., 2016. Biocompatibility and safety of PLA and its copolymers. Adv. Drug Deliv. Rev. https://doi.org/10.1016/j.addr.2016.03.012.

Ran, Q., Yang, W., Hu, Y., Shen, X., Yu, Y., Xiang, Y., Cai, K., 2018. Osteogenesis of 3D printed porous Ti6Al4V implants with different pore sizes. J. Mech. Behav. Biomed. Mater. 84, 1–11. https://doi.org/10.1016/J.JMBBM.2018.04.010.

Read, N., Wang, W., Essa, K., Attallah, M.M., 2015. Selective laser melting of AlSi10Mg alloy: process optimisation and mechanical properties development. Mater. Des. 65, 417–424. https://doi.org/10.1016/J.MATDES.2014.09.044, 1980-2015.

Singh, D., Babbar, A., Jain, V., Gupta, D., Saxena, S., Dwibedi, V., 2019. Synthesis, characterization, and bioactivity investigation of biomimetic biodegradable PLA scaffold fabricated by fused filament fabrication process. J. Braz. Soc. Mech. Sci. Eng. 41, 121. https://doi.org/10.1007/s40430-019-1625-y.

SolidWorks software [WWW document]. https://www.solidworks.com/, 1995.

Tan, C., Li, S., Essa, K., Jamshidi, P., Zhou, K., Ma, W., Attallah, M.M., 2019. Laser Powder Bed Fusion of Ti-rich TiNi lattice structures: process optimisation, geometrical integrity, and phase transformations. Int. J. Mach. Tool Manufact. 141, 19–29. https://doi.org/10.1016/J.IJMACHTOOLS.2019.04.002.

Ultimaker, 2010. Ultimaker Cura software [WWW document]. https://ultimaker.com/about-ultimaker.

Vallet-Regí, M., Arcos Navarrete, D., 2016. CHAPTER 1 biological apatites in bone and teeth. In: Nanoceramics in Clinical Use: from Materials to Applications (2). The Royal Society of Chemistry, pp. 1–29. https://doi.org/10.1039/9781782622550-00001.

Warnke, P.H., Douglas, T., Wollny, P., Sherry, E., Steiner, M., Galonska, S., Becker, S.T., Springer, I.N., Wiltfang, J., Sivananthan, S., 2009. Rapid prototyping: porous titanium alloy scaffolds produced by selective laser melting for bone tissue engineering. Tissue Eng. C Methods 15, 115–124. https://doi.org/10.1089/ten.tec.2008.0288.

Weiner, S., Traub, W., Wagner, H.D., 1999. Lamellar bone: structure–function relations. J. Struct. Biol. 126, 241–255. https://doi.org/10.1006/JSBI.1999.4107.

Zadpoor, A.A., 2015. Bone tissue regeneration: the role of scaffold geometry. Biomater. Sci. 3, 231–245. https://doi.org/10.1039/C4BM00291A.